CrossMark

Growth Mechanisms and Structural Properties of Lead Chalcogenide Films Grown by Pulsed Laser Deposition

I.S. VIRT,[1,2] I.O. RUDYI,[3] I. YE. LOPATYNSKYI,[3] YU. DUBOV,[4] Y. TUR,[1] E. LUSAKOWSKA,[5] and G. LUKA[5,6]

1.—Drogobych State Pedagogical University, Drogobych, Ukraine. 2.—University of Rzeszow, Rzeszow, Poland. 3.—Lviv Polytechnic, National University, Lviv, Ukraine. 4.—Ivan Franko Lviv National University, Lviv, Ukraine. 5.—Institute of Physics PAS, Warsaw, Poland. 6.—e-mail: gluka@ifpan.edu.pl

Three lead chalcogenide films, PbTe, PbSe, and PbS, with a high structural quality were grown by pulsed lased deposition (PLD). The films were grown on single crystal substrates (Si, KCl, Al_2O_3) and on Si covered with a Si_3N_4 buffer layer. The Si_3N_4 layer latter facilitated the lead chalcogenide layer nucleation during the first growth stages and resulted in a more homogeneous surface morphology and a lower surface roughness. The surface geometry (roughness) of the films grown on Si_3N_4 was studied by means of the power spectral density analysis. Different growth modes, ranging from plasma plume condensation to bulk diffusion, resulting in observed film morphologies were identified. The investigations were complemented by electrical characterization of the chalcogenide films.

INTRODUCTION

An increased interest in $A^{IV}B^{VI}$ compounds stems from their excellent ability to detect infrared (IR) radiation in a wide wavelength range. This explains practical applications of these compounds in various optoelectronic devices.[1–6] Lead chalcogenides (PbS, PbSe and PbTe) are especially good materials for mid-wave IR (wavelength of 2.5 μm) detection. They also have good chemical and mechanical stability. Especially promising for IR optoelectronics are $A^{IV}B^{VI}$ doped semiconductors and their solid solutions. The range of detection wavelengths can be extended, i.e. from mid-wave IR to far-IR region, by tin alloying. In addition, other systems such as HgCdTe are quite sensitive to crystal defects and, therefore, only HgCdTe single crystals are useful for efficient IR detection. In contrast to this, polycrystalline lead chalcogenides may exhibit higher sensitivity compared to their single crystalline counterparts.[7] This unique feature enables preparation of chalcogenide detector systems integrated with silicon technology. This integration illustrates a competitive advantage of lead chalcogenides over HgCdTe systems.[7,8]

Polycrystalline chalcogenide films grown by physical vapor deposition methods usually have n-type conductivity due to deviation from stoichiometry, i.e. due to excess lead or chalcogen deficiency.[9] The latter case can be an effect of lower adhesion of chalcogen atoms to the surface of the growing layer. PbSe films deposited from solution and used in commercial IR detectors often exhibit high stability, but there is a lack of information about the certain electrical parameters like free carrier concentrations in these films. Polycrystalline lead chalcogenide films like PbSe or PbS, exhibiting high IR sensitivity, usually have a microstructure composed of large size grains, from 0.4 μm to 0.9 μm. For comparison, nanocrystalline PbTe films with a grain size of 50–75 nm are more easily saturated with oxygen (by diffusion) and show good photosensitivity. In PbTe polycrystalline films, free carrier concentrations of 10^{18} cm^{-3} are usually reported.[9]

In this work, we obtained and studied lead chalcogenide films, PbTe, PbSe, and PbS, that were grown by pulsed laser deposition (PLD) and have

high structural quality. We analyzed the film structure, mechanical and electrical properties, as well as surface morphology of the deposited layers. Our aim was to acquire information about growth mechanisms and crystal structure formation of lead chalcogenides grown by PLD, which is one of the most prospective methods for lead chalcogenide film epitaxy.

EXPERIMENTAL

PbTe, PbSe, and PbS films were obtained by PLD using stoichiometric targets. The targets were prepared from Pb, S, Se, and Te elements having 5 N purity, and placed in quartz ampoules under vacuum to carry out the synthesis reaction. We used a YAG:Nd^{3+} laser with the following parameters: the laser wavelength was 1064 nm, the energy maximum in a pulse was 0.4 J, the power density was 4×10^8 W/cm^2, the pulse duration was 10 ns, and the pulse frequency was 0.5 Hz. The pressure inside the PLD chamber was 1×10^{-5} mm Hg, and the substrate temperature was 200°C. We used KCl(001), Si(111), and Si$_3$N$_4$/Si substrates. The latter substrates were prepared by depositing an Si$_3$N$_4$ buffer layer on Si(111) by PLD.[10–12] The Si$_3$N$_4$ layer thickness was 110 nm. The thickness of each lead chalcogenide film was 2 μm.

The structure and homogeneity of the synthesized PLD target materials were studied by x-ray diffraction (XRD) using a DRON-3.0 diffractometer with CuKα radiation and θ–θ scanning. The structural quality of the respective films was investigated by transmission high-energy electron diffraction (THEED) for the samples grown on KCl(001) substrates. We used an EMR-100 electron diffractometer with the acceleration voltages of 60–80 kV.

Surface morphology of the deposited films was investigated by atomic force microscopy (AFM; Nanoscope II, Veeco) in the tapping mode. AFM surface geometry (roughness) was studied by means of the power spectral density (PSD) analysis.[13,14] The PSD function, F_{PSD}, is the Fourier transform of the power function $P = h^2$ (nm^2), where h is the profile height at a given point. The investigated film lengths were $L = 2$ μm and the number of data points were $m = 512$. This gave the sampling distance $\Delta L = L/m \approx 3.9$ nm. Therefore, the lower and upper bandwidth of the F_{PSD} was 5×10^{-4} nm^{-1} and ≈ 0.26 nm^{-1}, respectively. The F_{PSD} data were fitted using the k-correlation model[14]

$$F_{PSD} = \frac{A}{\left(1 + B^2 (L^{-1})^2\right)^{\frac{C+1}{2}}} \quad (1)$$

where A, B, and C are the fit parameters.

Temperature-dependent electrical conductivities of the films grown on Al$_2$O$_3$(0001) substrates were measured in the 300–400 K range. We chose Al$_2$O$_3$ because of its good dielectric properties, good thermal conductivity and mechanical stability at a very
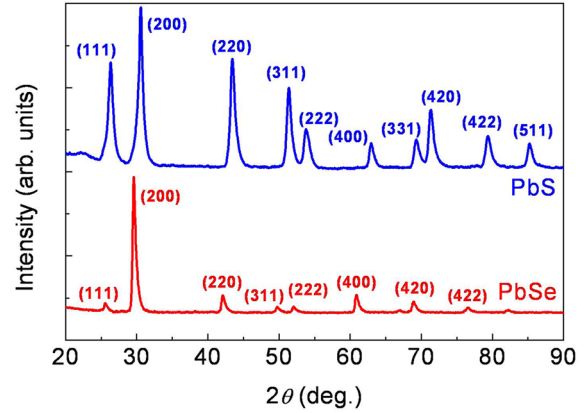

Fig. 1. XRD patterns of PbSe and PbS targets.

wide range of temperatures. For the measurements, silver metal contacts were thermally evaporated on the samples in vacuum through shadow masks. The activation energies E_a were calculated using the formula

$$\sigma(T) = \sigma_0 \exp\left(-\frac{E_a}{kT}\right) \quad (2)$$

where σ_0 is a constant, k is the Boltzmann constant and T is absolute temperature.

RESULTS AND DISCUSSION

The XRD patterns of PbSe and PbS target powders are shown in Fig. 1. The XRD pattern of PbTe target was already analyzed elsewhere.[15] All the patterns (including that of PbTe) indicate the presence of only one face-centered cubic phase of NaCl for all the materials. Additionally, there are no peaks corresponding to the precipitation of any compounds or binary alloys.[16–18] The calculated experimental interplanar distances d_{khl} are shown in Table I. They are very close to the standard data for bulk crystals.[19]

The THEED patterns of PbTe, PbSe, and PbS films deposited on KCl(001) substrates are shown and compared in Fig. 2. All the patterns consist of arced reflections corresponding to the Debye–Scherrer rings, according to the spread of grain orientations around the incident beam. From the patterns, we deduce that all the films contain one fcc phase of NaCl. However, a degree of texture differs among the respective films. In case of the PbSe films, we observe long arced reflections indicating a larger crystallite disorientation, compared to PbS and PbTe films. The diffraction pattern of the PbTe film is composed of short and blurry reflections placed on the Debye–Scherrer rings. The PbS layer shows the highest degree of texture. Here, short arced reflections with high intensity placed on the Debye–Scherrer rings are observed. The calculated lattice parameters are 6.462 Å, 6.117 Å, and 5.922 Å for PbTe, PbSe, and PbS films, respectively. They are

Table I. Interplanar distances d_{hkl} for the given (hkl) intensities of PbSe and PbS targets and films

	PbSe			PbS	
hkl	d_{hkl}, (Å) XRD target	d_{hkl} (Å) THEED film	hkl	d_{hkl} (Å) XRD target	d_{hkl} (Å) THEED film
1 1 1	3.4769	3.534	1 1 1	3.3830	3.422
2 0 0	3.0184	3.062	2 0 0	2.9228	2.971
2 2 0	2.1464	2.165	2 2 0	2.0833	2.094
3 1 1	1.8331	1.844	3 1 1	1.7782	1.782
2 2 2	1.7563	1.761	2 2 2	1.7050	1.706
4 0 0	1.5217	1.529	4 0 0	1.4772	1.479
3 3 1	1.3976	1.405	3 3 1	1.3620	1.378
4 2 0	1.3629	1.364	4 2 0	1.3270	1.366
$a_{(200)}$	6.114	6.117		5.927	5.922
a_{st}	6.124			5.936	
$\Delta a/a_{st}$	−0.16%	−0.11%		−0.15%	−0.24%

The values were derived from XRD (Fig. 1) and THEED (Fig. 2) data, respectively. The lattice constants, indicated as $a_{(200)}$, were calculated using d_{200} values. a_{st} are the standard values taken from Ref. 19. $\Delta a/a_{st} = \{[a_{(200)} - a_{st}]/a_{st}\} \times 100\%$.
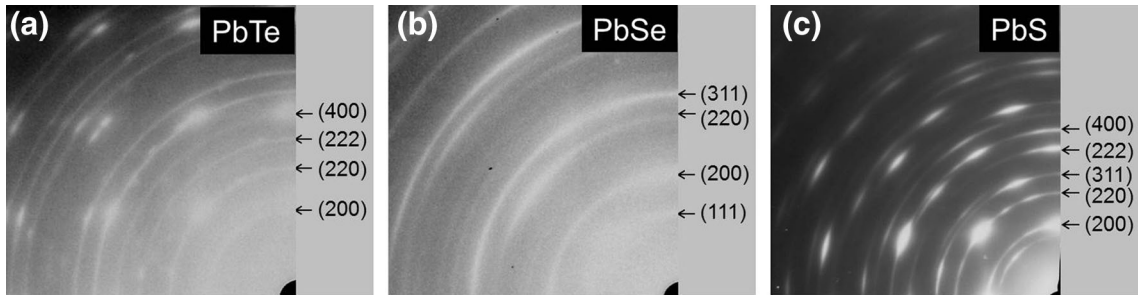

Fig. 2. THEED patterns of (a) PbTe, (b) PbSe, and (c) PbS films grown on KCl substrates. The most pronounced Miller indices (hkl) are indicated.

very close to the respective standard values a_{st} for powder diffraction of these materials.[19] The $\Delta a/a_{st}$ differences are −0.13%, −0.11%, and −0.24% for PbTe, PbSe, and PbS films, respectively. This means the presence of compressive strain in all the investigated films. Since the film lattice parameters were derived from the THEED measurements, we assume that the compression occurs in the film plane. We may estimate the lattice mismatch, $(a_{film} - a_{KCl})/a_{KCl}$, where a_{KCl} = 6.278 Å. The calculated lattice mismatch values are +2.2% for PbTe, −2.6% for PbSe, and −6.0% for PbS films. This estimation shows that the observed mechanical compression is not caused by the lattice mismatch. The standard lattice parameters for PbSe and PbS relaxed crystals are lower than the KCl lattice constant. This means that due to the lattice mismatch one should observe a mechanical tension in these two layers, in the film planar direction. Instead, a mechanical compression is observed. This is a result of interactions between the atoms within the layer rather than between the layer atoms and the substrate atoms. To analyze this quantitatively,

we determined mechanical parameters of the chalcogenide layers. The stress σ was calculated using the following equation

$$\sigma = \frac{E}{1 - v} \times \frac{a - a_{st}}{a_{st}} \quad (3)$$

where E is the Young modulus and v is the Poisson ratio. The values of E and v[20] as well as the calculated values of σ are gathered in Table II. The mean dislocation distance, $\langle L \rangle$, was calculated using the equation $\langle L \rangle = |\boldsymbol{b}|/\varepsilon$, where $|\boldsymbol{b}| = a/2^{1/2}$ is the value of the Burgers vector and $\varepsilon = \Delta a/a_{st}$.[21] The density of dislocations, N, that form at the growing layer/substrate interface is then equal to $(1/\langle L \rangle)^2$. A degree of relaxation, $R = (a_{film} - a_{KCl})/(a_{st} - a_{KCl})$, can be estimated for the deformation occurring in the film plane. The estimated values of $|\boldsymbol{b}|$, $\langle L \rangle$, N, and R are shown in Table II. From the calculations, it follows that the most stress-sensitive layer is PbS. This is not only related to the Young modulus but also to the dislocation density. The latter is associated with much higher strain values

Table II. Mechanical parameters of the investigated films grown on KCl(001) substrates

Layer	E (GPa)	v	a (Å)	$\Delta a/a_{st}$ (%)	σ (MPa)	$|b|$ (Å)	$\langle L \rangle$ (nm)	N $(10^6/mm^2)$	R
PbTe	61.02	0.38	6.427	−0.13	−128	4.544	350	8.1	0.98
PbSe	66.33	0.33	6.117	−0.11	−109	4.326	393	6.5	0.99
PbS	66.48	0.32	5.922	−0.24	−234	4.188	175	33.2	1.04

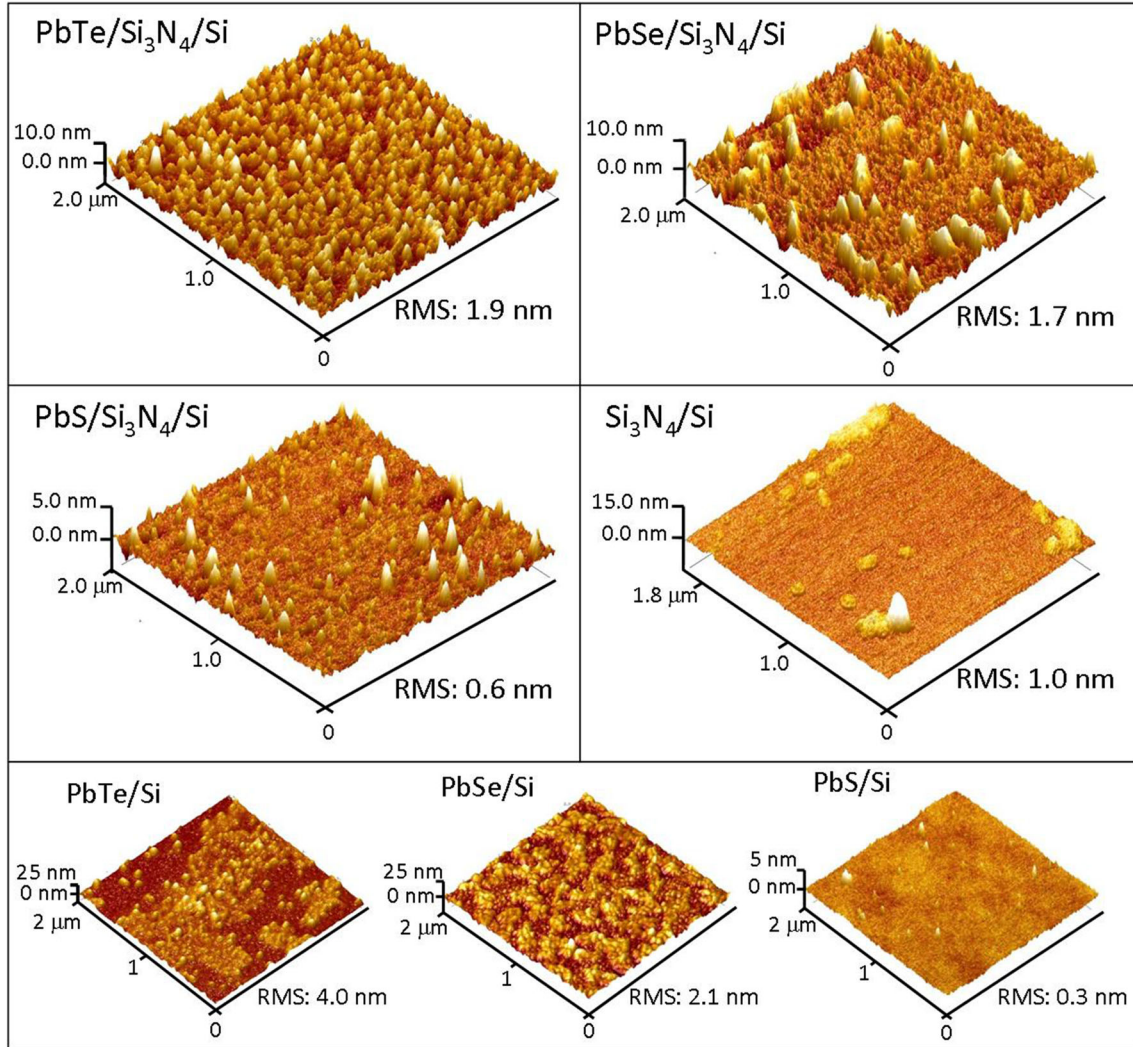The E and v values (for bulk crystals) are taken from Ref. 20.

Fig. 3. (Top) AFM surface morphology of: PbTe, PbSe, and PbS films, grown on Si_3N_4/Si(111) substrates, and the Si_3N_4/Si(111) substrate. (Bottom) AFM images of PbTe, PbSe, and PbS films grown on Si(111). RMS surface roughness values are indicated.

for the PbS film than in case of the other investigated chalcogenide layers. We also observe the following relations: the higher the degree of texture (crystallinity), the higher density of dislocations and the higher the strain. This indicates that in more polycrystalline films, the formation of grains and the presence of an atomic disorder at the grain boundaries constrain the dislocation formation at

the first growth stages and reduce the strain during the prolonged layer growth.[22]

Figure 3 shows AFM images of PbTe, PbSe, and PbS film surfaces. The films were grown on Si(111) substrates and Si(111) covered with the 110-nm-thick Si_3N_4 buffer layer. The Si_3N_4 layer has the root mean square (RMS) roughness ≈1 nm. However, grains or islands with the lateral size

(diameter) $\leq \approx 100$ nm are infrequently observed. From comparing the grain structures of the layers grown on Si ans Si_3N_4/Si substrates, we conclude that the Si_3N_4 layer facilitated nucleation of lead chalcogenides at their first growth stages. The moderate roughness of Si_3N_4, that is obviously higher than the atomically smooth Si surface, resulted in a creation of new crystallization centers, most probably at boundary regions between Si_3N_4 grains. The resulting surface morphology of the films deposited on Si_3N_4 is also more homogeneous and contains lower amounts of larger atom aggregates (clusters), compared to the respective layers grown on Si. This is apparent in the case of the PbTe and PbSe films while the PbS is an exception. Additionally, the surface roughness of the films deposited on Si_3N_4 decreased. The RMS roughnesses of PbTe, PbSe, and PbS films deposited on Si were 3.3 nm, 2.1 nm, and 0.3 nm, respectively. The films deposited on Si_3N_4/Si under the same conditions showed the respective RMS values: 1.9 nm, 1.7 nm, and 0.6 nm. The PbS layer deposited on Si already had very low surface roughness. Here, the RMS value did not decrease further and the Si_3N_4 layer had no impact on the atom aggregates' formation.
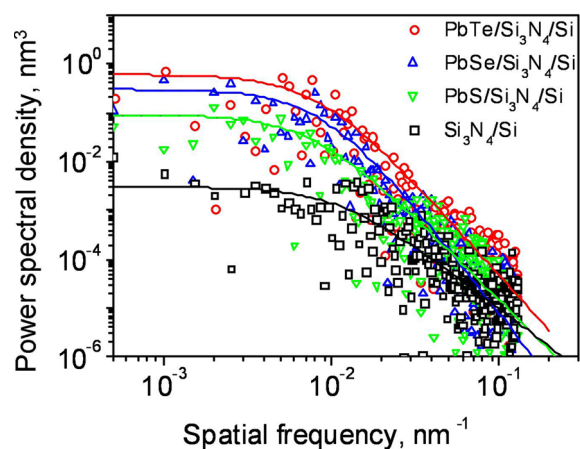

Fig. 4. Open symbols: power spectral density (PSD) of the PbTe, PbSe, PbS, and Si_3N_4 surface profiles, determined from the AFM data. Lines: the results of fitting data (open symbols) by Eq. 1.

Surface morphologies of the investigated films were studied more in detail by the PSD analysis of their surface profiles. The calculated PSD function (F_{PSD}) values for the PbTe, PbSe, and PbS layers grown on Si_3N_4/Si substrates, as well as the F_{PSD} of the Si_3N_4 surface profile, are shown in Fig. 4 (open symbols). The F_{PSD} data were fitted by Eq. 1. The fit results are shown in Fig. 4 (lines). The fit parameters A, B, and C are gathered in Table III. The A parameter, corresponding to the F_{PSD} values for lower spatial frequencies f (i.e. the plateau regions for $f < \sim 10^{-2}$ nm^{-1}), is the lowest for the Si_3N_4 layer. It increases for the PbS, PbSe, and PbTe layers, respectively. These f values correspond to average lateral distances of the order of 0.1 μm and higher. They may be associated with regions having similar morphology and distinct from regions of the size $< \sim 0.1$ μm with different morphologies. The B parameter, corresponding to the knee of the F_{PSD} versus f fit lines, is similar for PbSe, PbTe, and PbS layers (110–130 nm), and slightly lower (90 nm) for the Si_3N_4 layer. For $f > \sim 10^{-2}$ nm^{-1}, i.e. for lateral sizes lower than 100 nm, the F_{PSD} function decreases. A measure of this decrease is the C parameter. Its value is related to the inverse slope of the F_{PSD} function. According to Refs. 14, 23, and 24, the $C = 1$ indicates a growth mode associated with the viscous flow whereas $C = 2$, $C = 3$, and $C = 4$ are related to condensation, bulk diffusion, and surface diffusion, respectively. For PbS and PbTe films, the growth mode is between condensation and bulk diffusion ($C = 2.4$ and $C = 2.8$, respectively). For PbSe, $C = 3.3$ relates to the growth mode between bulk and surface diffusion. At the PbSe surface, we observe single two-dimensional aggregates with the size of ~ 200 nm. According to the above analysis, formation of the aggregates was conditioned by the contribution of the species in the whole layer. A different situation occurs for the PbS film growth, where larger aggregate formation is associated mostly with condensation of the arriving plasma plume species at the PbS surface.

Finally, we complement our investigations by electrical characterization of the lead chalcogenide layers, grown on sapphire substrates. We carried out temperature-dependent conductivity measurements. The results are shown in Fig. 5 as the

Table III. Fit parameters A, B, and C of the power spectral density Eq. 1

Layer	A (nm^2)	B (nm)	C
PbTe/Si_3N_4/Si	0.6	120	2.8
PbSe/Si_3N_4/Si	0.3	110	3.4
PbS/Si_3N_4/Si	0.09	130	2.4
Si_3N_4/Si	0.003	90	1.6

The parameters were obtained by fitting Eq. 1 with the PSD of the surface morphologies of the investigated chalcogenide layers (see Fig. 4).
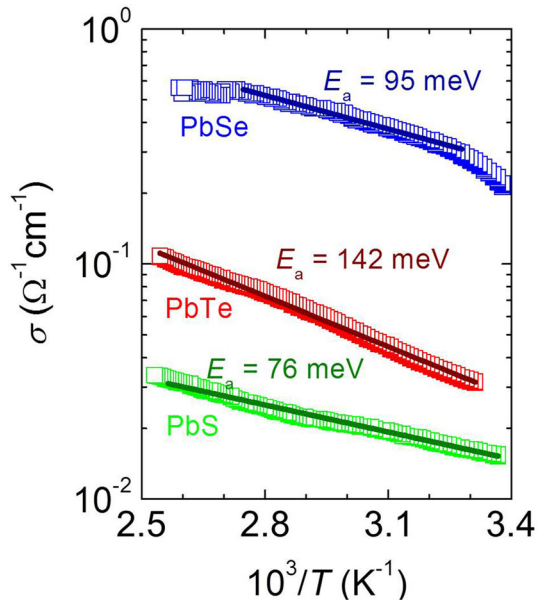
Fig. 5. Temperature dependence of the electrical conductivity of the PbTe, PbSe, and PbS films, measured in the 300–400 K range.

conductivity σ versus inverse temperature T^{-1} in a semi-log scale. The highest conductivity at room temperature (RT) was achieved by PbSe, $\approx 0.2 \ \Omega^{-1} \ cm^{-1}$. PbTe and PbS layers have lower conductivities at RT, $\approx 0.03 \ \Omega^{-1} \ cm^{-1}$ and $0.015 \ \Omega^{-1} \ cm^{-1}$, respectively. These conductivity values at RT are inversely related to the respective energy gaps of the investigated materials. Experimentally determined energy gaps for PbSe, PbTe, and PbS are 0.26–0.29, 0.29–0.32, and 0.37–0.40 eV, respectively.[25,26] This indicates that at temperatures close to RT, the intrinsic conduction dominates. The observed activation-type $\sigma(T)$ behavior, with determined activation energies of 76–142 meV, is associated with the presence of deep donor states. Most probably, these states are generated by Se, Te, or S vacancies in the respective films.[25] Such vacancies can form during the PLD growth due to different sticking coefficients of chalcogen and lead adatoms.

CONCLUSIONS

We obtained lead chalcogenide films, PbTe, PbSe and PbS, by the PLD method. The layers show good structural quality. The degree of texture slightly varied among the three chalcogenides and was the highest for the PbS layer. The highest structural order of PbS was associated with the smoothest surface morphology, the highest density of dislocations that formed at the film/substrate interface, and the highest compressive strain in the film plane direction. The latter two phenomena were attributed to the relatively low density of grain boundaries that could constrain the dislocation formation and reduce the strain. At the surface of the lead chalcogenide films, atoms form aggregates (clusters). In case of the PbSe and PbS films, the density of these aggregates decreased when an additional layer of Si_3N_4 was deposited on Si before lead chalcogenide film deposition. The PSD analysis of the film surface profiles indicated different mechanisms of larger aggregate formation during the PLD growth. In PbS and PbTe films, larger aggregates formed predominantly by the condensation of an arriving plasma plume species at the film surface. For PbSe, additional bulk diffusion processes within the layers contributed to the resulting surface geometry. The investigations were complemented by electrical measurements of the deposited films. At room temperature, the electrical conductivity is associated mostly with the intrinsic conduction which is related to different energy gaps of these materials. In addition, activation behavior of the $\sigma(T)$ dependencies indicated a contribution of deep energy states (donors) generated by chalcogenide atom vacancies.

OPEN ACCESS

REFERENCES

1. B. Weng, J. Qiu, L. Zhao, Z. Yuan, C. Chang, and Z. Shi, *Proc. SPIE* 8993, 899311 (2013).
2. J. Wang, T. Zens, J. Hu, P. Becla, A.M. Agarwal, and L.C. Kimerling, *Proc. SPIE* 8034, 80340K (2011).
3. V. Kasiyan, Z. Dashevsky, C.M. Schwarz, M. Shatkhin, E. Flitsiyan, L. Chernyak, and D. Khokhlov, *J. Appl. Phys.* 112, 086101 (2012).
4. C. Sierra, M.C. Torquemada, G. Vergara, M.T. Rodrigo, C. Gutiérrez, G. Pérez, I. Génova, I. Catalán, L.J. Gómez, V. Villamayor, M. Álvarez, D. Fernández, M.T. Magaz, and R.M. Almazán, *Sens. Actuators B* 190, 464 (2014).
5. M.C. Torquemada, V. Villamayor, L.J. Gómez, G. Vergara, M.T. Rodrigo, G. Pérez, I. Génova, I. Catalán, D. Fernández, R.M. Almazán, M. Álvarez, C. Sierra, C.M. Gutiérrez, M.T. Magaz, and J. Plaza, *Sens. Actuators A* 199, 297 (2013).
6. B. Weng, J. Qiu, L. Zhao, C. Chang, and Z. Shi, *Appl. Phys. Lett.* 104, 121111 (2014).
7. J. Wang, J. Hu, P. Becla, A.M. Agarwal, and L.C. Kimerling, *J. Appl. Phys.* 110, 083719 (2011).
8. S. Kouissa, A. Djemel, M.S. Aida, and M.A. Djouadi, *Sens. Transducers* 193, 106 (2015).
9. YuI Ravich, B.A. Efimova, and I.A. Smirnov, *Semiconducting Lead Chalcogenides* (New York: Plenum Press, 1970).
10. I.O. Rudyi, I.V. Kurilo, M.S. Frugynskyj, M. Kuzma, J. Zawislak, and I.S. Virt, *Appl. Surf. Sci.* 154–155, 206 (2000).
11. I.S. Virt, T.P. Shkumbatyuk, I.V. Kurilo, I.O. Rudyi, T. Ye, Lopatynskyi, L.F. Linnik, V.V. Tetyorkin, and A.G. Phedorov, *Semiconductors* 44, 544 (2010).
12. I.S. Virt, I.O. Rudyj, I.V. Kurilo, I.Y. Lopatynskyi, L.F. Linnik, V.V. Tetyorkin, P. Potera, and G. Luka, *Semiconductors* 47, 997 (2013).
13. S. Singh and S. Basu, *Surf. Coat. Technol.* 201, 952 (2006).

14. T. Itoh and N. Yamauchi, *Appl. Surf. Sci.* 253, 6196 (2007).
15. I.S. Virt, Y. Tur, I.O. Rudyi, I.Y. Lopatynskyi, M.S. Frugynskyi, I.V. Kurilo, E. Lusakowska, B.S. Witkowski, and G. Luka, *J. Cryst. Growth* 432, 19 (2015).
16. X. Sun, K. Gao, X. Pang, H. Yang, and A.A. Volinsky, *Appl. Surf. Sci.* 356, 978 (2015).
17. S. Prabahar, N. Suryanarayanan, K. Rajasekar, and S. Srikanth, *Chalcogenide Lett.* 6, 203 (2009).
18. J. Qiu, B. Weng, Z. Yuan, and Z. Shi, *J. Appl. Phys.* 113, 103102 (2013).
19. H.C. Casey Jr. and M.B. Panish, *Heterostructure Lasers. Part B: Materials and Operating Characteristics* (Academic Press, New York, 1978).
20. A. Bali, R. Chetty, R.C. Mallik, and A.I.P. Conf, *Proc.* 1591, 1118 (2014).

21. E. Wintersberger, N. Hrauda, D. Kriegner, M. Keplinger, G. Springholz, J. Stangl, G. Bauer, J. Oswald, T. Belytschko, C. Deiter, F. Bertram, and O.H. Seeck, *Appl. Phys. Lett.* 96, 131905 (2010).
22. W.D. Callister and D.G. Rethwisch, *Materials Science and Engineering: An Introduction*, 9th ed. (Hoboken: Wiley, 2014).
23. D.G. Stearns, P.B. Mirkarimi, and E. Spiller, *Thin Solid Films* 446, 37 (2004).
24. W.M. Tong and R.S. Williams, *Annu. Rev. Phys. Chem.* 45, 401 (1994).
25. W.-F. Li, Ch-M Fang, M. Dijkstra, and M.A. van Huis, *J. Phys.: Condens. Matter* 27, 355801 (2015).
26. W.H. Strehlow and E.L. Cook, *J. Phys. Chem. Ref. Data* 2, 163 (1973).